Author/s:
Phukan, M;Jyoti, A;Black, JR;Haese, RR

Title:
Changes in Pore Geometry and Connectivity in the Basalt Pore Network Adjacent to Fractures in Response to CO2-Saturated Fluid

Date:
2021-12-01

Citation:
Phukan, M., Jyoti, A., Black, J. R. & Haese, R. R. (2021). Changes in Pore Geometry and Connectivity in the Basalt Pore Network Adjacent to Fractures in Response to CO2-Saturated Fluid. Water Resources Research, 57 (12), https://doi.org/10.1029/2021WR030275.

Persistent Link:
https://hdl.handle.net/11343/299250

Changes in pore geometry and connectivity in the basalt pore network adjacent to fractures in response to CO_2-saturated fluid

Meghalim Phukan[1], Apoorv Jyoti[1], Jay R. Black[1] Ralf R. Haese[1]

[1] Peter Cook Centre for CCS Research, School of Geography, Earth and Atmospheric Sciences, The University of Melbourne, Parkville, VIC, Australia 3010

Corresponding author: Meghalim Phukan (meghalim.phukan@unimelb.edu.au)

Key Points:

- The geometry of the connected pore network changed post reaction
- Pore and throat size distribution changed with a higher reduction of pores than throats, and overall porosity decreased
- Mineral dissolution and precipitation occurred concurrently, the volume of precipitated mineral is larger than the dissolved volume

This is the author manuscript accepted for publication and has undergone full peer review but has not been through the copyediting, typesetting, pagination and proofreading process, which may lead to differences between this version and the Version of Record. Please cite this article as doi: 10.1029/2021WR030275.

Abstract

Pores connected to fractures provide an increased surface area for fluid-rock interactions when reactive fluids, such as CO_2-saturated water, flow within fractures. Diffusion-controlled transport of ions including dissolved CO_2, Ca^{2+}, Mg^{2+}, Fe^{2+} and Si within the connected pore network can lead to local mineral undersaturation or supersaturation and respective local dissolution or precipitation of secondary minerals. In this study, a diffusion-controlled experiment was conducted on a fractured basalt under sub-surface conditions (60°C and 80 bars) to investigate the changes in the pore volume, the connectivity within the pore network, the pore and throat size distribution and to quantify the volume of dissolved and precipitated mineral phases. CO_2-saturated water with a supply of ions from the dissolution of basalt powder was reacted with an artificially fractured basalt sample over 12 weeks. The net pore volume of the sample decreased by 158 mm^3, equivalent to 7.7 % of the initial pore volume (2041 mm^3). The number of pores decreased considerably (15 %) while the decline in the number of throats was small (4 %) suggesting precipitation primarily occurred in pores. The number of isolated pores declined, which is attributed to mineral dissolution leading to greater connectivity within the pore network. Overall, the results provide insights into the early phase of reactive fluid flow in fractured basalt eventually leading to self-sealing of fractures and the adjacent pore network.

1 Introduction

Basalt formations are often fractured, which poses the risk of CO_2 leakage from a geological CO_2 storage reservoir. Despite their fractured nature, basalts are considered for large-scale CO_2 injection and storage due to large potential storage capacity and rapid carbon mineralisation (Matter et al. 2016, McGrail et al. 2016, Xiong et al. 2018). The advantage of fractures is the connectivity to a larger pore network adjacent to fracture surfaces, which provide a large mineral reactive surface area for chemical reactions, and may play a dominant role in changing the porosity of basaltic rock. Mineral precipitation in fractures and connected pores could act as a self-sealing process in the case of a CO_2 leakage from a CO_2 storage reservoir, thus reducing the risk of the long-term leakage of CO_2. Mineral precipitation in basalt fractures has been observed in natural analogue systems where hydrothermal fluids have migrated upwards through basalts over geological time (Eggleton et al. 1987, Rogers et al. 2006, Goldberg et al. 2008). However, a range of factors including the flow velocity of the CO_2-enriched plume, fluid chemistry, pressure and

temperature conditions and the fracture aperture size need to be considered in order to predict the rate and extent of the potential self-sealing of fractures (Brunet et al. 2016).

Several laboratory studies have been performed to understand the influence of transport limitations on the extent of mineral formation and pore network alterations in natural basalt cores when exposed to acidic CO_2-rich fluids under relevant geologic storage conditions (Adeoye et al. 2017, Xiong et al. 2017, Menefee et al. 2018). Experimental flow studies conducted by Luhmann et al. (2017a) at 150°C and 15 MPa pCO_2, and Adeoye et al. (2017) at 45-100°C and 10 MPa pCO_2 both observed no carbonate mineral precipitation. Luhmann et al. (2017a) observed Si- and Al-rich phases leading to permeability reduction, while net mineral dissolution was detected in the latter case due to a short residence time. Experiments involving artificially fractured basalt core samples at 100°C and 150°C and 10 MPa pCO_2 observed the formation and uneven distribution of carbonate mineral in the zones where the solute transport was diffusion-controlled (Xiong et al. 2017, Xiong et al. 2018). Menefee et al. (2018) studied the extent of carbonation under different flow regimes at 100°C and 150°C and 10 MPa pCO_2 using $NaHCO_3$ as a buffer and a source of carbonate ions. Their study showed that mineralization predominantly occurred at higher temperature in the diffusion-limited zones adjacent to the bulk flow path. The CO_2-enriched acidic fluid reacts within the fracture, leading to the mobilization of cations and their diffusion into pores connected to the fracture as a function of the concentration gradient. Once fluid within the pores becomes supersaturated with respect to certain minerals, local mineral precipitation may occur. Therefore, these studies demonstrated mineral dissolution occurs where advection controls solute transport, while diffusion-controlled zones within the pore network play an important role in mineral carbonation in the context of geological carbon storage in basalts. Previous diffusion-controlled mineral carbonation experiments have had long incubation periods, artificial carbonate ion supply, very shallow fracture depths (100 μm) and high alkalinity conditions (Xiong et al. 2017, Luhmann et al. 2017a, Luhmann et al. 2017b, Menefee et al. 2018, Xiong et al. 2018). Therefore, the nature of CO_2-saturated fluid-basalt interactions facilitated by fracture flow under reasonable storage conditions and early stage of geochemical reactions remains poorly understood.

The CO_2 storage potential and changes in the pore network of basalts have been identified and quantified in several experimental studies, for example, by determining the net precipitation/dissolution volume and by analysing the location of the mineral precipitation (Xiong et al. 2017, Luhmann et al. 2017a, Callow et al. 2018, Menefee et al. 2018, Xiong et al. 2018). 1D

and 2D continum scale reactive transport models have been developed by using pre- and post-experimental micro-CT data, which predicted carbonate mineral precipitation in the diffusion-limited regions as early as 1 day after addition of CO_2 due to the build-up of dissolved cations in the dead ends of fractures (Xiong et al. 2017, Menefee et al. 2018). Pore network models derived from micro-CT data provide insight into the pore and throat size distribution and pore connectivity. Gharbi et al. (2013) studied the impact of CO_2 injection and mineral reactions in a carbonate rock using a pore scale model on micro-CT data. The number of pores and throats in their specimen decreased at high flow velocity due to wormhole formation caused by grain dissolution.

The concurrent and potentially coupled processes of mineral dissolution and precipitation need to be considered in order to fully assess the geochemical changes in a fractured basalt with CO_2-rich or supercritical CO_2 fluids infiltrating the fracture network. Coupled dissolution and precipitation processes can significantly modify the connected fracture network. For example, Singurindy and Berkowitz (2005) investigated the influence of fractures on the evolution of hydraulic conductivity caused by the dissolution of calcium carbonate and precipitation of gypsum in carbonate rocks. Rocks with rough fracture surfaces clogged more rapidly, causing a reduction in the overall conductivity and porosity (Singurindy and Berkowitz 2005, Huerta et al. 2012).

The objective of this study is to better understand the influence of the early stage of geochemical reactions on preferential fluid flow pathways (faults and fractures) and their adjacent pore network. This study aimed to observe dissolution and precipitation processes in the zone adjacent to fault and fractures, where transport is diffusion limited and the pH is low. Changes in the pore network geometry are quantified in terms of pore connectivity, pore and throat size, and changes in the solid phase volume fraction. An experiment was conducted at P/T conditions representing a depth of approximately 800 m in the sub-surface using an artificially fractured core with approximately 2 millimeter deep grooves. The core was immersed in a fluid continuously receiving a supply of ions analogous to a natural fluid flow system. Changes in the connected pore network (CPN), the pore and solid phase volume and the surface area were analyzed using non-destructive imaging technique (X-ray micro-CT). Pore and throat size distribution of the pre- and post-experimental basalt sample were mapped and quantitatively compared. Most importantly, the total volume of mineral dissolution and precipitation was calculated and changes in the volume of the CPN were estimated. This study thus gives new insight into the processes and conditions important for the consideration of geological CO_2 storage in fractured basalt reservoirs. In particular, the self-sealing

capacity of fractures and the associated pore network due to secondary mineral precipitation as a consequence of the interactions between basalt and CO_2-saturated fluid are studied.

2 Materials and Methods

2.1 Experimental method

A sample of massive continental flood basalt was sourced from the Bambstone Bluestone quarry in Port Fairy, Australia. The major primary minerals (plagioclase, pyroxene, alkali feldspar and olivine) and chemical compositions of the basalt was determined by standard methods (Phukan et al. 2021) and is presented in the Supporting Information (Table S1and S2).

A core with a diameter of 25.6 mm and 60 mm length was drilled out from a sample block by using an automated plugging machine (Vinci Technologies) and cut lengthwise into two halves with a rock saw. Four grooves with a diameter of 2 mm and a depth between 1-2 mm were milled into the surface of one half core (Fig.1a) using a mini drill (Dremel 3000) with a 2 mm diamond bur. The core surface was wiped with ethanol to remove any stains and then sonicated in water before being oven dried at a temperature of 40°C for 2 days. The half core samples were glued together by applying Master Bond EP42HT-2 epoxy on the clean outer edges along the length of the core. Any remaining gaps were filled with more adhesive. The glued core sample was left to cure for 12 hours at room temperature and 3-5 hours in an oven at 65°C. The outer core surface was impregnated with a layer of epoxy to avoid any reaction, and similar curing procedures were followed. After the curing process, PTFE tape was wrapped around the core as an additional protective layer.

A high pressure Hastelloy C 5500 Compact Mini Bench Top 450 mL Parr® Reactor was used to conduct the geochemical reactions of basalt core with CO_2-saturated water. The internal parts of a conventional Parr® Reactor set-up consists of a dip tub, cooling loop, impeller and a thermocouple, which were modified for this study (Fig.1b). To accommodate the assembled core inside the reactor and avoid corrosion, a core holder made of high-grade stainless steel (T316 SS) was designed. The core was fit in-between two disks connected to each other by six long stainless steel screws. A disk at the top and bottom of the core have openings in the centre and connect tubing with the grooved core. The injected CO_2 flows through the top disk into the grooves of the core and leaves the core through the bottom disk of the core. Thereafter, it mixes with the surrounding

experimental fluid. The dip tube of the reactor was shortened and connected to the inlet of the core holder (Fig.1b). The dip tube was used for CO_2 injection and for fluid sampling. The cooling loop and the impeller were removed to fit the core holder.

Prior to the main fractured core experiment (M-core), two baseline batch experiments (B-1 and B-2) were performed in a 450 mL Parr® reactor to determine the supply of dissolved ions through the dissolution of basalt powder in a nylon bag (See Supporting Information, Text S1). In the baseline and the M-core experiments basalt powders with a grain size fraction of 90 to 125 µm was placed inside nylon bags and immersed in deionised water (DI). The bags were sealed at the top with a nylon thread of same material. The mesh size of the nylon diffuser bag was 90 microns, i.e. the grain size of the basalt powder was kept larger than the mesh size of the nylon diffuser bag. The sealed nylon bags were sonicated in DI water and acetone three times each to remove any fine particles. This process was done to ensure no loose particles escape the diffuser nylon bags during the experiment. The mineral saturation state based on the evolution of the water composition in the baseline experiments was used to decide on an optimal mass of basalt powder as a source of dissolved ions in the M-core experiment. The core in the M-core experiment was incubated with 250 mL of DI water. The core and the core holder assembly were fully immersed with a headspace of 80 mL maintained. In order to reach mineral supersaturation in the fluid quickly, three nylon bags with a a total of 38 grams of powdered massive basalt were placed under water in the reactor adjacent to the core holder assembly (Fig.1c). The nylon diffuser bags provided a constant resupply of ions to the pore network adjacent to the grooves where mineral reactions occur. This experimental system is meant to replicate a natural analogue situation as closely as possible.

The rock to water (r:w) wt. ratio in the M-core experiment was 0.152 (excluding the exposed core fracture), which is 10 times and 3.7 times higher compared to experiments B-1 and B-2, respectively. Higher r:w ratio in the main experiment was used to achieve a higher secondary mineral saturation in the fluid, which was not achieved in the baseline experiments. The diffuser bags were placed on either sides and on the top of the core holder assembly.

The temperature of the M-core experimental reactor was set to 60°C. The CO_2 gas from the cylinder was used to purge the reactor at 2 bars for 30 minutes to remove the residual oxygen from the fluid prior to the experiment. The CO_2 gas from the cylinder was transferred to a syringe pump (500D, Teledyne Isco) to add pressurized CO_2 to the headspace. Once the CO_2 line was opened,

supercritical CO_2 flowed through the grooves from the top of the core and encountered the surrounding fluid from the bottom opening of the core holder. The reactor vessel was then finally pressurized to 85 bars. The solubilty of CO_2 at 85 bars and 60°C is 0.9 mol/kg (Duan and Sun 2003). The CO_2 concentration will be same inside the grooves and outside of the core. Reactions are expected to be slow inside the grooves due to a smaller surface area compared to the basalt powder in the nylon diffuser bags.

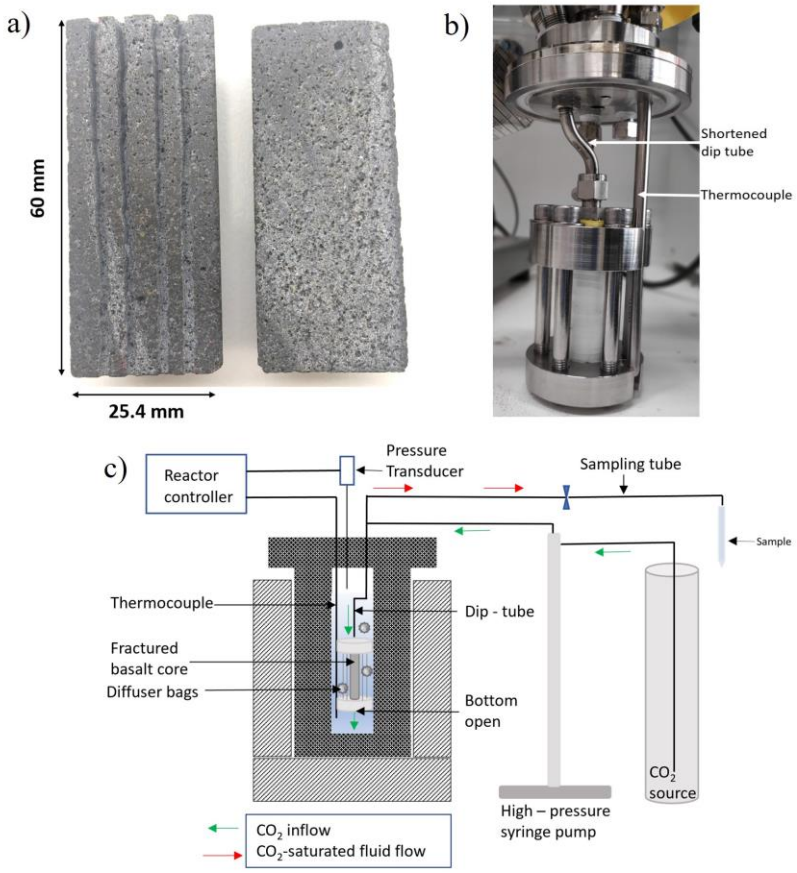

Figure 1: (a) Massive basalt core with four grooves serving as fluid flow pathways analogue to fractures (b) Assembled core, core holder and shortened dip tube connecting to the assembled core top (c) Schematic representation of the static M-core experiment

A total of 50 ml of fluid was collected as ~10 mL aliquots through the shortened dip tube and regulated through the high-pressure sampling valve after 1, 4, 14, 50 and 86 days. The operation included represurization of the system with CO_2 back to 85 bars after every sampling, which leads to the homogenosation of the fluid and fresh mixed fluid is drawn into the grooves and interacts with with the pore network adjacent to the grooves before the next fluid sample is taken. The fluid

sample represents a mixed fluid sample from outside and inside of the core. After an incubation period of 12 weeks, the reactor was cooled down and slowly depressurized before it was opened.

The core was immediately rinsed with DI water to remove any fine particles from the surface of the core and was air dried for 10 days. Fluid samples from the baseline and the M-core experiments were filtered with a pore size of 0.45 μm and acidified with 2 % HNO_3 acid before major and minor cations, and Si were analysed.

2.2 Analytical methods

2.2.1 Fluid analysis and solid-phase analysis

Aqueous samples from the baseline and M-core experiments were analysed by inductively coupled plasma optical emission spectrophotometer (ICP-OES) to measure the major ion concentrations (Ca^{2+}, Mg^{2+}, Fe^{2+}, Na^{+}, K^{+}, Si, and Al^{3+}). Total alkalinity analysis was performed using a potentiometric titration method (916 Ti- Touch titrator, Metrohm) on unfiltered and non-acidfied aqueous samples. Porosity of a different massive basalt bulk core from the same rock sample without grooves (L = 48 mm; D = 37 mm) was also measured by the weight difference between the dry and the water-saturated core (Safiuddin and Hearn 2005) as shown in the Supporting Information (Text S3).

2.2.2 Micro-CT analysis of the core

The pre- and post-experimental core was imaged using a GE Phoenix Nanotom M micro-CT scanner (Waygate Technologies) operated using the xs control and phoenix datos|x acquisition software. The analysis of high-resolution core images using the micro-CT helps in determining the physical changes of the core post-reaction (Xiong et al. 2017, Luhmann et al. 2017a, Callow et al. 2018, Menefee et al. 2018). In order to obtain an optimum scan, operational parameters are required to be optimised by accounting for the size and the type of the sample. The main parameters adjusted are the power of the X-ray and the distance of the sample from the source.

An important factor in X-ray imaging is the resolution of a scan, as it defines the voxel size in the 3-dimensional reconstructed data. Features such as pores, pore throats and solid grains below the scanned resolution are not detected. In this study, the samples were scanned at a resolution of 14.99 μm. Scans were acquired using a voltage of 110 kV, a current of 350 μA collecting 2000 x-ray

projections through a full 360 degrees of rotation of the sample for 72 minutes (average of 3 images with 1 skip image and integration time of 0.5 seconds per projection). A 0.1 mm copper filter was used to pre-harden the x-ray beam. The optimised resolution in the field-of-view captured the full width of the core and a height of ~20 mm on the detector, thus 4 scans were collected along the length of the core to capture its full length with some overlap to allow scans to be registered and stitched together after scanning. The reconstructed data was imported and processed in the Avizo® software package (Thermo Fisher Scientific) with the pore network modelling expansion. When working with pre- and post-experimental images, aligning the two data sets into the same coordinate system is an important step known as registration. The pre-experimental image is taken as a reference and the post- image is transformed to match it. This is a two-step process, first an initial alignment is achieved manually and then the automatic registration algorithm of Avizo is applied. In our study, microfractures were observed at the top and bottom of the core in the post-experimental CT image (Text S6) . The cause of the microfractures is not clear, but it could be due to excessive pressure imposed by the core holder on the core while being set-up. Due to the observed microfractures in the post-experimental core image, the analysis and registration of the pre- and post-experimental images of the whole core was not viable as the original spatial location of the grains and the pores were shifted in the post-experimental core. Therefore, the pre- and post-experimental images of the two half cores (grooved and the un-grooved sides) were registered separately and the analysis was limited to the mid-section (40 mm) of the two half cores.

After registration, segmentation of pores and grains is the next step in the processing of the datasets. In our study, we have used the auto thresholding algorithm of Avizo to get an initial threshold of the dataset. This algorithm computes an automatic threshold on a grey scale image; here, we made use of the factorization method based on the Otsu criterion (Otsu 1979). Following the initial automatic segmentation, segmentation was further improved by visual feedback using the interactive threshold tool in Avizo. Three sub-regions were selected randomly in the unreacted image and the porosity was computed.(See Supporting Information, Figure S4). However, the measured porosities were not perfectly validated. The total segmented porosity in the micro-CT data of the whole core (9.75%) is less than the porosity measured by the saturation method (12%, Supplementary Text S3). This is expected due to limitiations of the resolution of the micro-CT data (Tutolo et al. 2020). However, changes to the pore-network above the limits of micro-CT resolution can still be evaluated. The threshold value for the reacted image is very close to the

unreacted image, and a sensitivity analysis shows a variation in segmented porosity of around +/- 1% within reasonable threshold limits of the segmentation point.

Numerical algorithms available in the Avizo software were used to quantify physical changes between the pre- and post-experimental samples, which are elaborated on in the following sections. Porosity, grain volume, and surface area of the core halves were extracted individually. Avizo's Axis Connectivity module was used to analyse the change in connected pore network (CPN). A pore network model (PNM) was also generated to analyse the change in pore and throat size. Changes in the solid phase volume fraction due to mineral dissolution and precipitation were quantified for both cores halves.

2.2.2.1 Porosity, total surface area and grain volume analysis

Porosity (Eq.1) is the ratio of the pore voxels to the total numbers of voxels, and it can be estimated as:

$$\emptyset = \frac{n_{pore}}{n_{pore} + n_{mineral}} \quad (1)$$

where, $\emptyset$ is the porosity, n_{pore} is the number of voxels assigned to the pore space, and $n_{mineral}$ is the number of voxels assigned to the mineral phases.

For calculating the total surface area, Avizo's VoxelFaceArea analysis is used. This value is the sum of voxel surfaces that are on the outside of the each connected component (Avizo 2018). Similarly, the total volume of the a phase (Eq.2) is calculated as the product of the number of voxels assigned to the that phase (a_{voxel}) and the volume of each of these voxels V_{voxel}(Avizo 2018) according to

$$V_i = \sum_{i=0}^{n} a_{voxel_i} . V_{voxel} \quad (2)$$

Where a is either a mineral or a pore phase.

2.2.2.2 Connected pore network structure (CPN)

As the focus of the experiment was to observe the changes in the grooves and adjacent pore network due to mineral reactions, the CPN was isolated from the dataset of the grooved half core and analysed separately. To separate the CPN, the axis connectivity module in Avizo was used. The grooves give full connectivity to the network if the orientation matches the direction selected in the axis connectivity module. Therefore, it was implemented in the z-direction, which is the orientation of the grooves. The CPN in the unreacted and the reacted sample were extracted from the grooved-half core segmented pore volumes. The pre- and post-experimental CPN was used to analyse its volumetric and the geometric changes. The axis connectivity module was also implemented on the un-grooved side of the core, but failed to generate any results due to the absence of fractures leading to no connectivity in the z-direction.

The unreacted CPN was subtracted from the reacted CPN in order to estimate the volume of the new pore network connection by grain dissolution. This algorithm does not quantify the net volume of dissolution or precipitation; however, it determines the volume of the previously isolated pore network in the unreacted sample, which is now connected in the post-experimental reacted sample by grain dissolution. In contrast, the reacted CPN was subtracted from unreacted CPN to estimate the volume of the disconnected blocked pathways by mineral precipitation. Similarly, the previously connected part of the pore network in the unreacted sample is now lost due to mineral precipitation by blocking small pores and throats.

2.2.2.3 Pore network model (PNM)

PNMs are used for the topological equivalent representation of a porous media. A PNM was generated for the un-grooved half core, which allows a complex porous rock to be represented using simpler shapes in the form of balls and sticks representing pores and pore connections without losing out on the original topological properties of the rock. This is done by computing watershed lines on the binarized image. This method is a high-level combination of the watershed, distance transform, and numerical reconstruction algorithm (Doroszko and Seweryn 2017, Ramos and Matouš 2018, Ahmed and Lebedev 2019). The first step is constructing a chamfer distance map, which represents the minimal distance of a voxel from the pore boundary. The higher intensity represents bigger pores, and the low intensity represents smaller pore. This distance map is used as a priority map input for the watershed process. The most inner areas of the pores, which are the maxima areas in the distance maps are used as markers in the watershed process. Avizo's

Seperate Objects module is used for this analysis. The output from this module is a separated pore image with a unique label assigned to each pore. The separated pore image is taken as an input for constructing the PNM.

The PNM is constructed using Avizo's pore network module, which uses the watershed method to segment pores by starting from regions of higher intensity in the chamfer distance map and filling pores until a phase boundary is encountered in a gradient map. The throats of the network are defined by the locations where the segmentation of two different pores converge. Subsequently, the volume of the pores and the surface area of the throats are calculated. The ideal pore is a sphere with an equivalent volume of the irregular shaped real pore, and the ideal throat is a cylinder with an equivalent surface area as the irregular shaped real throat. The output from this analysis is a histogram of the frequency of the pore and throat size distributions quantified in bins across the range of detected sizes (Avizo 2018). This analysis was only conducted on the un-grooved half of the core. As the grooves could not be divided into pores and throats, therefore did not yield any results

2.2.2.4 Quantification of dissolved and precipitated minerals

In order to quantify the volume of the dissolved and precipitated minerals in the grooved and the un-grooved half cores, a logical AND arithmetic operator was used to compare segmented image overlap (Fig. 2). This arithmetic operator works as a logic gate with a true/false filter. For quantification of dissolution in the dataset, this logic gate when applied to the unreacted mineral image ($V_{UR}^{minerals}$) and the reacted pore image (V_R^{pores}), constructs a new voxelised image where there is overlap between the final pore space and the initial mineral phase indicating regions where mineral solid phase either dissolved or dislodged (Fig. 2 left hand operation). As the reaction was diffusion limited, this difference is taken as dissolution ($V_R^{secondary\ pores}$).

The AND logic gate was applied to compare the reacted mineral image ($V_R^{minerals}$) and the unreacted pore image (V_{UR}^{pores}), which allowed the quantification of precipitation. A voxelised image was derived showing the new solid phase within the reacted core (i.e. mineral precipitation, $V_R^{precipitate}$) where pore space initially occurred in the uncreacted core (Fig. 2 right hand operation). The grey images in Figure 2 give a 2D pictorial representation of the mineral volume lost by dissolution or formed by secondary precipitation.

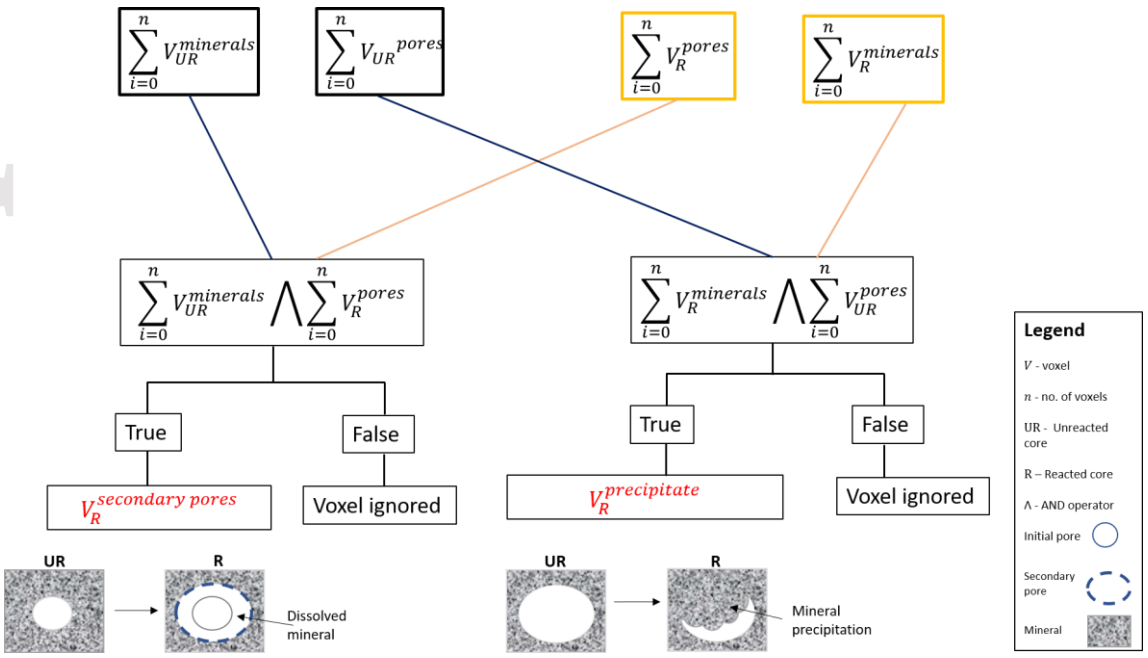

Figure 2. Flow chart showing the algorithm and steps used to separately quantify the total volume of dissolved and precipitated minerals in the half cores

2.3 Geochemical modelling

Aqueous speciation and the respective state of mineral saturation was calculated for the baseline and the main core experiments using Geochemist's Workbench 11.0 (GWB) to understand whether certain minerals are under- or supersaturated at certain times during the experiment (GWB11 2016). Mineral saturation indices were computed for each fluid sample using the updated thermo.comV8.R6+ database. The following equation gives the mineral saturation index SI

$$\mathrm{SI} = Log\left(\frac{Q}{K}\right) \tag{3}$$

where Q is the ion activity product, and K is the mineral specific equilibrium constant.

The equilibrium constants of the identified solid solution minerals in the basalt sample were calculated using GWB endmembers and ideal mixing. The database was modified and thermodynamic data of andesine and augite were included. The CO_2 (aq.) concentration in the speciation model was calculated from the CO_2 solubility at the temperature and pCO_2 of the experiment using the Duan and Sun model (Duan and Sun, 2003) . The pH is calculated based on the charge balance.

3 Results

3.1 Fluid chemistry

No fluid discolouration or suspended matter was observed after opening the reactor at the end of the baseline and the M-core experiments. The concentration differences between the two baseline experiments with different r:w ratios were compared as a function of time (Supporting Information, Text S1).

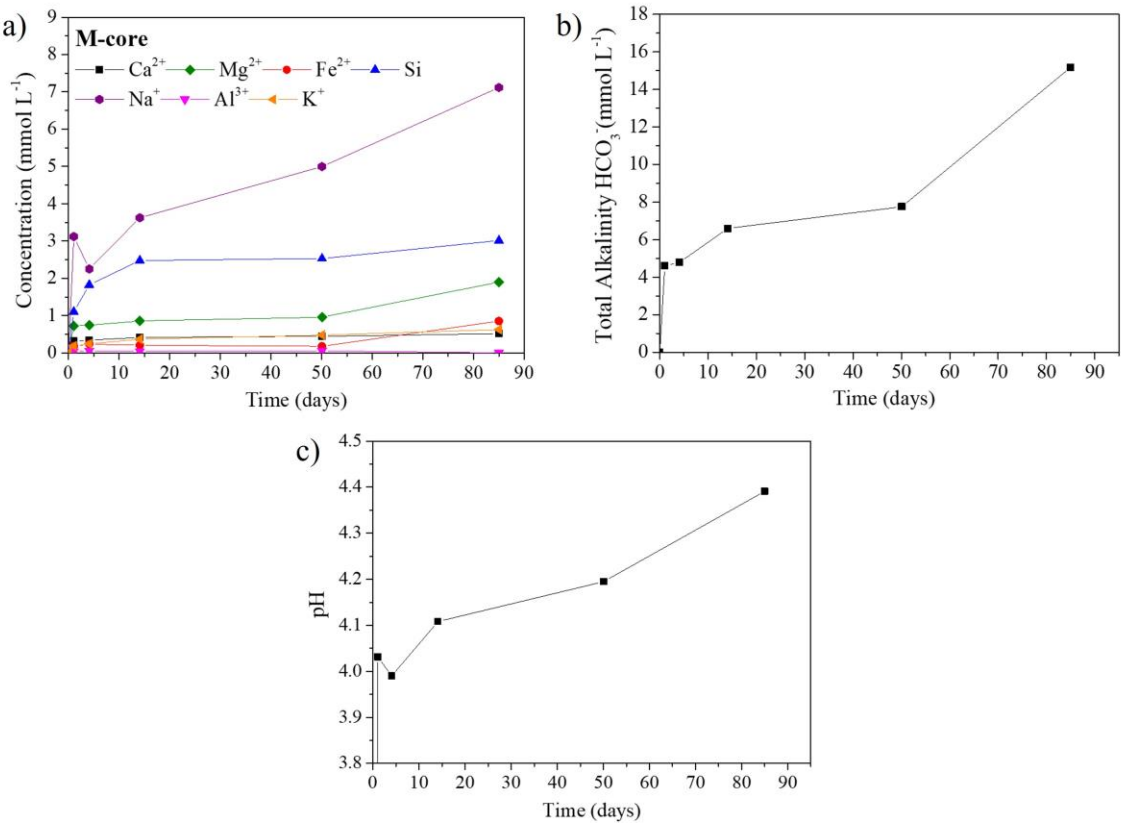

Figure 3: Fluid chemistry of the core experiment (a) Major cation concentrations in the fluid, (b) total alkalinity, and (c) calculated pH of the fluid over a period of 86 days

Figure 3 presents the change in cation concentrations, alkalinity, and pH of the M-core experiment over 85 days. The enrichment of dissolved ions is expected to be mostly caused by mineral dissolution in the basalt diffuser bags, while the influence of the exposed areas at the top and the bottom of the core and the grooves within the core is considered to be minor. The concentration of Mg^{2+}, Fe^{2+}, and Si increases until day 14, then plateaus until day 50, and then again increases

until the end of the experiment. The increase in dissolved Na^+ over time suggests a high net release from primary minerals, while the net Si release is only half of the Na release.

3.2 State of mineral saturation

The last fluid sample concentration of the baseline experiments was used to compute the mineral saturation indexes. Mineral saturation states are computed for major primary minerals (a), clay minerals, chalcedony and amorphous silica (b), zeolites (c), and carbonate minerals (d). The mineral saturation states at the end of the baseline experiments are presented in the Supporting Information (Text and Figure S2).

The state of mineral saturation of the M-core experiment was calculated stepwise over the incubation time and results are shown in Figure S3. Primary minerals (olivine, augite, andesine) were strongly undersaturated or near equilibrium $\log(Q/K) \leq 0$. K-feldspar, clay minerals (kaolinite, smectite, illite) were supersaturated $\log(Q/K) > 0$ and SiO_2 variations (chalcedony, amorphous silica) were near equilibrium $\log(Q/K) \approx 0$. Within the group of zeolites, stilbite was supersaturated while mesolite and mordenite became supersaturated after day 4. All the carbonate minerals show a similar trend, but remain undersaturated throughout the experiment, only siderite was at equilibrium at the end of the experiment.

The state of saturation of zeolites in the M-core experiment increased significantly over the first 15 days compared to the saturation state of carbonate minerals. The state of saturation of the highly supersaturated clay minerals and zeolites showed a declining trend towards the end. The degree of supersaturation increased steadily for zeolites and clay minerals until day 10 which may indicate mineral nucleation. The state of saturation plateaued between day 15 to 50, which may suggest a period of mineral growth. After day 50, the saturation state of the two mineral groups decreased again. Amorphous SiO_2 is in equilibrium throughout the experiment and the state of saturation of beideillite was higher than for kaolinite. The precipitation of clay minerals such as smectite and zeolites such as stilbite leads to the production of H^+ and the consumption of certain cations and alkalinity as shown in Equations 4 and 5. The fluid composition outside the core, however, shows opposite trends which is explained by the high rate of basalt powder dissolution. In other words, dissolution of primary minerals within the nylon bags and precipitation of secondary minerals within the core occur concurrently, with the dissolution reactions dominating the trend in the water

composition. The importance of the balance between dissolution and precipitation reactions in controlling changes in water composition was demonstrated earlier for basalts (Phukan et al. 2021).

$$0.165Mg^{2+} + 2.33Al^{3+} + 3.67SiO_{2(aq)} + 4.66H_2O = Mg_{0.165}\,Al_{2.33}Si_{3.67}O_{10}(OH)_2 + 7.32\,H^{+} \quad (4)$$

(Beideiilite-Mg)

$$0.006K^{+} + 0.136Na^{+} + 1.019Ca^{2+} + 2.18Al^{3+} + 6.82SiO_{2(aq)} + 11.69H_2O = Ca_{1.019}\,Na_{0.136}K_{0.006}Si_{6.82}O_{18}{:}\,7.33H_2O + 8.72H^{+} \quad (5)$$

(Stilbite)

3.3 X-ray micro-CT results

The pre- and post-CT scan data were used to separately determine the porosity, grain volume, and surface area of the grooved and the un-grooved half cores. The total pore volume was reduced from 2041 mm^3 to 1883 mm^3 within the area of investigation during the experiment equivalent to reduction of 7.7%. The net porosity changes of both half cores are presented with respect to distance from the inlet (core top) in Figure 4b.

The trend of net porosity change is similar for both grooved and the un-grooved halves (Fig. 4b). The negative values in the net porosity change (%) in Figure 4b indicates that there was a net mineral precipitation, showing peaks at 17.5 mm and 40 mm from the inlet of the core. In the post-experimental half-cores, porosity is reduced in the slices on average by 0.5 % and 1 % in the grooved and the un-grooved half cores, respectively.

The net total grain volume increased by 0.75 % and 1.3 % in the grooved half core and un-grooved half core, respectivly. The increase in the net grain volume is attributed to net precipitation, which is in agreement with the described decrease in porosity. The total surface area of the grains in the grooved half-core decreased by 4.89 %. The change in grain surface area in the un-grooved half core is more significant than in the grooved half core with a reduction of 10.6 % observed. As the two half cores are considered as one entity (a fractured core) in the study, the net grain volume increases by 158 mm^3, and an equivalent amount of the total pore volume is lost.

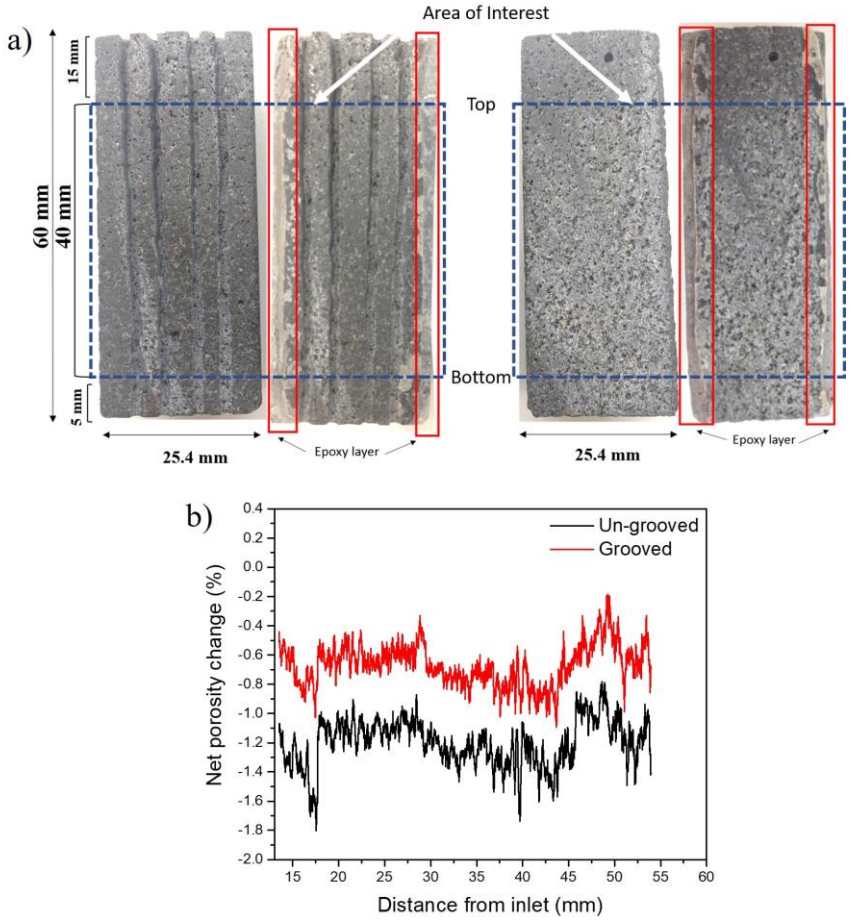

Figure 4: a) Comparison of the pre- and post- experimental grooved and un-grooved half cores. The area within the blue stripped line is the area of interest (b) Net porosity change percentage (post-pre porosity) of the grooved and un-grooved half cores CT images

The total volume of primary mineral dissolution and secondary mineral precipitation in the two half-cores were quantified separately using Avizo's AND arithmetic operator by comparing the unreacted to the reacted cores, as shown in the flowchart in Figure 2 (Section 2.2.2.4). A slice in the x-y direction (perpendicular to the length axis of the core), at 21 mm from the top of the core is extracted and used for an explicit demonstration of how the AND operator was used to quantify the dissolution and precipitation during the experiment (Supporting Information, Text S5). The CT data was used to create 3D-segmentation of the pre- and post-experimental half-cores. Figure 5 shows the greyscale image of the initial grains, segmented initial pores, and dissolved and precipitated minerals of the grooved half-core. The grains (minerals) and the pores are represented by different greyscale values (Fig. 5a and 5b). Figure 5c and 5d shows the segmented 3D image of the dissolved grains and the precipitated minerals, respectively, after the experiment. The initial

grains are dissolved, and secondary minerals formed in the initial pores due to fluid-rock interactions. In the grooved half-core, a volume of 145 mm^3 of secondary minerals formed within the initial pore volume of 1295 mm^3, and only a volume of 77.4 mm^3 of the initial primary minerals dissolved. In the un-grooved half-core, a total of 113 mm^3 minerals precipitated and only a volume of 21 mm^3 dissolved. Consequently, the total volume of mineral dissolution and precipitation in the whole core is 98.4 mm^3 and 258 mm^3, respectively. The net precipitation is 158 mm^3, which is about 1.6 times higher than the volume of dissolved minerals.

The 3D pore axis connectivity was segmented out from the grooved half-core and analysed separately. The initial CPN volume is 40 % of the total porosity (CPN volume + isolated pore volume) which is 518.10 mm^3. A net reduction of 4 mm^3 of the CPN volume was observed in the post-experimental core which is < 1 % of the initial CPN volume, suggesting blockage of pores by mineral precipitation was not important. However, the geometry of the CPN changed, and a new structure was observed in the post-experiment sample. New pore clusters (connected pores) were observed in the reacted CPN, while a few old pore clusters no longer existed (Fig. 6a). Callow et al. (2018) suggested the connected porosity is a significant parameter to calculate CO_2 reservoir storage capacity, as isolated pores do not allow permeation of CO_2-saturated fluid and hence should be ignored with regards to CO_2 storage. However, our study shows that connected porosity changes during the reaction process. The impact of fluid-rock interaction on the CPN is very dynamic. New fluid pathways are opened due to the grain dissolution, and the neighbouring isolated pores or pore clusters can become connected to the primary pore network. Simultaneously, some initially connected pores were blocked due to mineral precipitation, so that they became isolated from the primary CPN. The volume of isolated pores and clusters in the grooved half-core reduced by 8 % during the experiment.

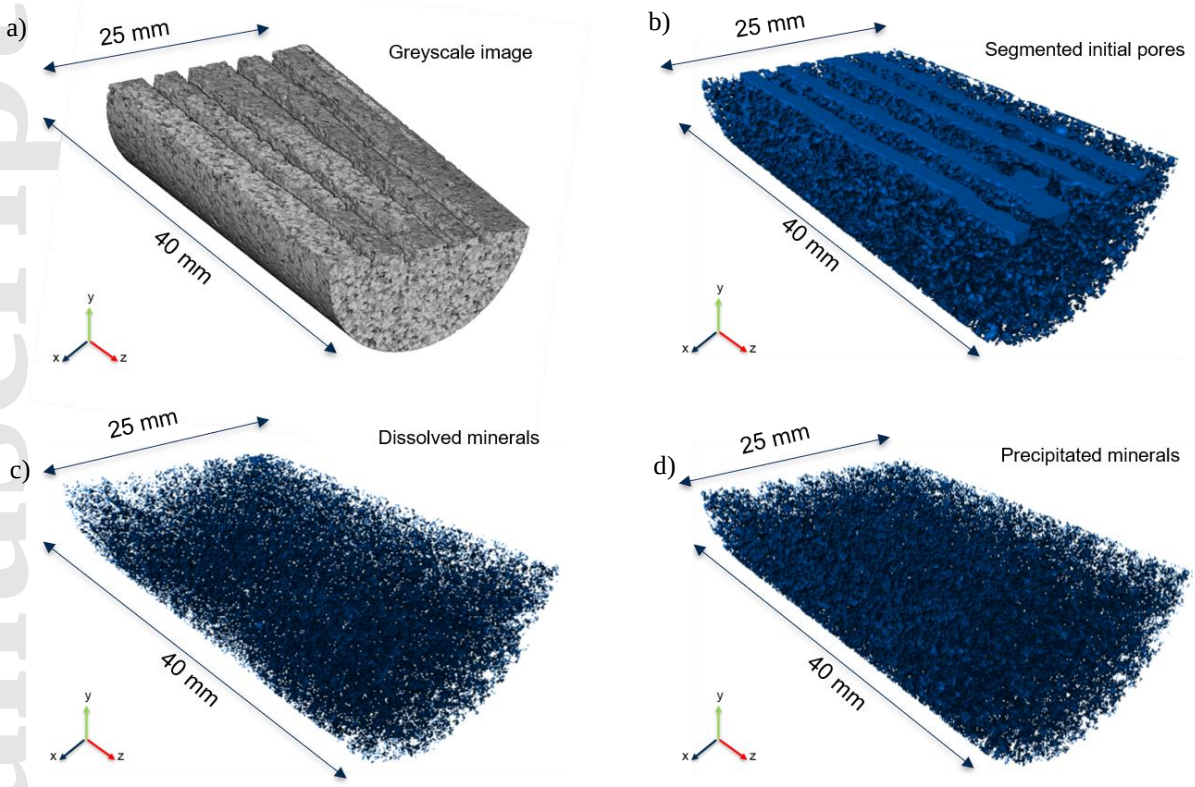

Figure 5: CT images of the grooved half core (a) initial greyscale image of the grooved half core, (b) segmented initial pores (c) dissolved minerals and (d) precipitated minerals; Images (c) and (d) were derived using the AND arithmetic operator algorithm for all the slices (section 2.2.2.4)

One may expect pore throats to be modified to a greater extent than pores due to dissolution or precipitation given the larger surface area to volume ratio of throats compared to pores. The images of the pre- and post-experimental CPN were superimposed to identify the spatial locations and calculate the volume of new and blocked pore connections. To estimate the volume of newly opened pathways, the reacted CPN was subtracted from unreacted CPN and vice versa for blocked pathways. The volume of new CPN is 13.4 mm^3 and the volume of blocked or disconnected pore volume is 17.8 mm^3 after the experimental duration. Figure 6 also highlights the areas where precipitation impacted a large cluster of pores which were disconnected from the reacted CPN. Figure 6b and 6e shows the size of the blocked pores due to mineral precipitation in the reacted micro-CT image, which led to the blockage of previously connected pathways. Figures 6c and 6f show the unreacted pore image where pore clusters remain connected to the main network. Figure 6d and 6g show the reacted pore image where the connections of the pore clusters are now missing due to mineral precipitation occurring.

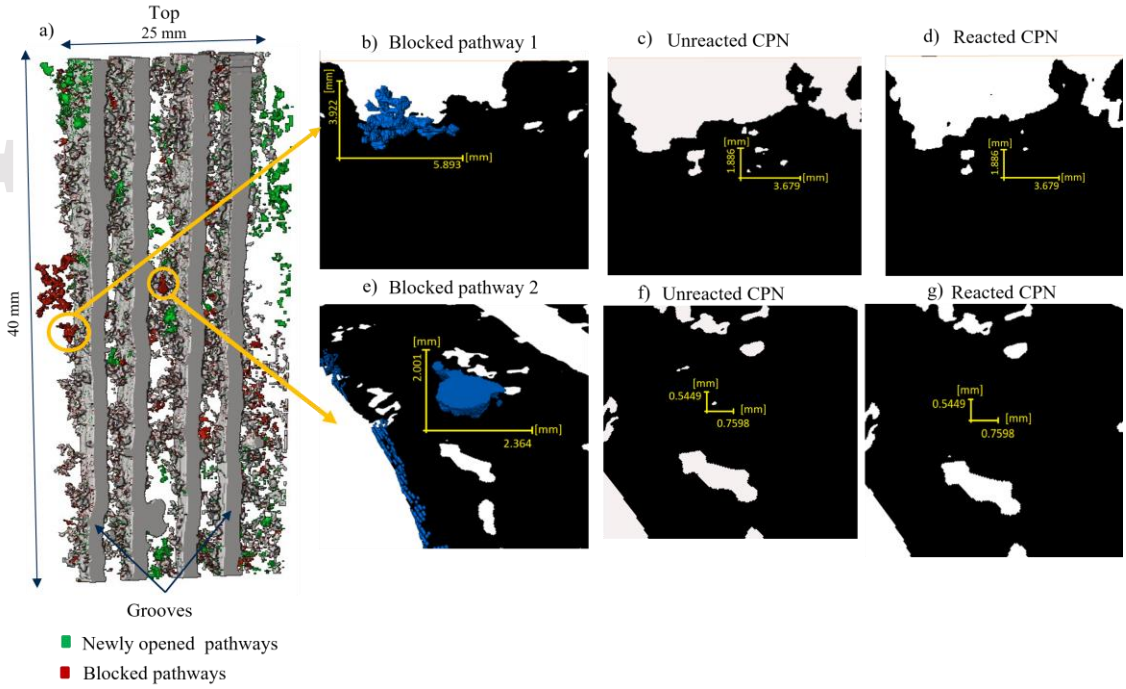

Figure 6: a) Change in total CPN. b) and e) size of the mineral precipitates blocking the pore clusters (red-encircled in yellow) in the reacted CPN, c) and f) initial open pore size within the scale bar in the unreacted CPN image (white), d) and g) blocked pore size within the scale bar in the reacted CPN image.

The PNM was generated for the pre- and post-experimental un-grooved half-core to calculate the net change in the total number of pores and pore throats. Figures 7a and 7b show the greyscale images of the unreacted un-grooved half-core and of the segmented total pores, respectively. Figure 7c shows the separated and voxelised pores where different colours represent individual pores. Intermediate steps (Fig. 7a, 7b, and 7c) and the final PNM (Fig. 7d) of the un-grooved core are shown in Figure 7 (see Figure 7 caption for a colour legend). Similarly, the PNM was generated for the post-experiment un-grooved half core. In total, there was a reduction of 12090 pores and 506 throats, which is 15 % of the initial pores and 4.4 % of the initial throats, respectively. Moreover, the PNM also calculated the number of isolated pores that are not connected by any throats. A significant reduction of 15 % was observed in the isolated pores in the post-reacted un-grooved half core. It is interesting to note the reduction in isolated pores at a greater distance from the grooves.

Figures 7e, 7f, and 7g shows the wide distribution of pore radii and throat radii in the pre- and post-experimental un-grooved half-core. The data from the PNM was placed in equally spaced

bins representing the pore and the throat sizes, and the number of pores and throats per bin was calculated. An initial increasing trend is observed in Figures 7e, 7f, and 7g, and after attaining a peak, it gradually declines with an increase in the pore and throat size. Figure 7e shows a normal distribution for the number of connected pores (coordination number >1) per bin in the range of 0.05 and 0.50 mm with a maximum at 0.15 mm. More than 80% of pores are in the range of 0.11 to 0.24 mm. In Figure 7f, a normal distribution for the number of unconnected pores (coordination number = 0) is shown in the range of 0.01 and 0.20 mm with a maximum at 0.03 mm. More than 80% of pores are in the range of 0.01 to 0.07 mm, which is distinctively smaller than the range of connected pores. In contrast, Figure 7g shows a bimodal distribution for the number of throats per bin in the range of 0.01 to 0.10 mm with maxima at 0.03mm and 0.06 mm. The blue line in Fig. 7e, 7f and 7g shows the difference between the unreacted and the reacted pores/throats in the un-grooved samples. The number of unconnected pores is more than 10 times larger than throats in both the unreacted and reacted samples, whereas connected pore frequency is similar to throat frequency.

In the PNM, there are some bins where dissolution and others where precipitation can be seen. The majority of the pores with a radius > 0.1 mm show some precipitation occurring with a maximum in precipitation at a pore radius of about 0.2 mm (Figure 7e). On the other hand, predominantly smaller pores within the unconnected pore distribution (Figure 7f) were impacted by precipitation. For example, a significant reduction of 23 % of pores (≈ 4500 pores) with a radii of 0.02 mm was observed in the reacted sample (Figure 7f). Majority of throat with a radius < 0.15 mm reduced in the reacted sample (Figure 7g). It is important to note that the given ranges in pore and throat radii exceed the micro-CT scan resolution of 14.99 μm or 0.015 mm.

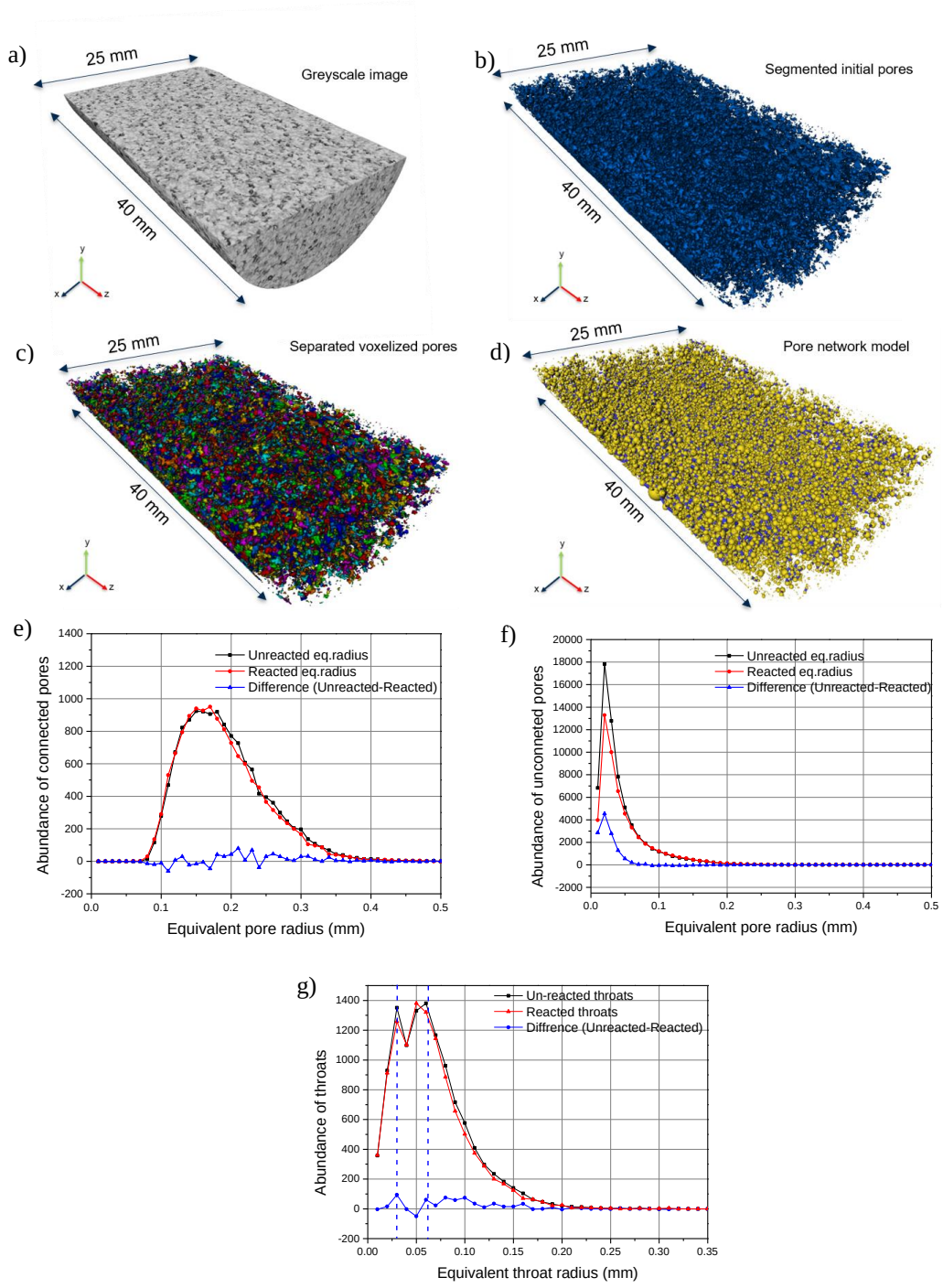

Figure 7: Workflow for the development of PNM consisting of pores and throats of the un-grooved core before experiment. (a) initial grey scale image of the un-grooved half core (b) initial total pores (c) pore separation of connected pore space (d) the PNM distinguishing of the pores (yellow) and throats (blue). Abundance of (e) connected pores, f) unconnected pores and g) throats of the unreacted and reacted un-grooved half core sample. The blue line in Fig. e, f and g represents the difference between unreacted and reacted un-grooved samples

4 Discussion

4.1 Changes in water composition

Changes in the water composition within a closed system reflect the balance between the release of ions through mineral dissolution, for example, and the consumption of ions through mineral precipitation. The balance of dissolution and precipitation reactions can change over time. A fluid can initially be undersaturated relative to potential secondary minerals, but precipitation of minerals may commence later once the concentrations of dissolved ions exceed the point of mineral saturation. The mineral mass and surface area was approximately 3 times larger in baseline experiment B-2 compared to B-1, therefore, a significantly more rapid increase in dissolved ions was expected in experiment B-2 assuming mineral dissolution greatly exceeds precipitation. However, only dissolved Na was found to reach 3-times higher concentrations in B-2 compared to B-1 (Supporting Document). The calculation of the state of saturation for potential secondary minerals suggests that kaolinite, certain smectites and chalcedony and/or amorphous silica could precipitate after 8 days of incubation in baseline experiments. Therefore, mineral precipitation most likely limited the increase in dissolved ions. Another factor could be that the growth of smectites increased the sorption capacity of the system, potentially taking the divalent cations out of the fluid compared to monovalent cations.

The release of Na^+ is expected to result from the dissolution of fine K-feldspar matrix. Xiong et al. (2018) observed a higher release rate of Na compared to Si and suggested incongruent dissolution as a cause where proportionally more Na than Si was released from the Na-matrix. In their experiment, the Na concentration was ≈ 50 mmol/L, while Si only reached a concentration of 3 mmol/L after 6 weeks. Alternatively, if congruent dissolution of primary minerals prevails, nucleation and growth of secondary minerals can control the evolution of the water composition (Phukan et al. 2021). In this case, preferential precipitation of Si over Na^+ could lower the Si concentration in the fluid. The low Si, Mg, and Fe concentrations in experiment B-2 suggests sorption of divalent ions and precipitation of Mg-Fe silicates. Si is usually rapidly incorporated into Si-rich secondary phases, forming a layer on top of the primary mineral (Sissmann et al. 2014, Hellevang et al. 2017, Menefee et al. 2018, Wolff-Boenisch and Galeczka 2018). The undersaturated state of carbonate minerals under these two different r:w ratios of the baseline

experiments suggest that the cation concentrations and the low pH were not favourable conditions for the formation of carbonate minerals over 7 days.

The r:w ratio in the M-Core experiment was 3- and 10-times larger than in B-2 and B-1 experiments, respectively, and the M-Core incubation time was 85 days. The SI of kaolinite was lower than beideillite in the main core experiment. This could be due to the higher precipitation rate of kaolinite compared to beideillite. The saturation state of amorphous SiO_2 in the M-core could also reflect concurrent precipitation. Previous studies observed formation of amorphous SiO_2 (Gysi and Stefánsson 2012c, Menefee et al. 2018). Contrary to the baseline experiments, several zeolite minerals were supersaturated over most of the incubation period. Particularly, stilbite, a Ca-rich zeolite, was highly supersaturated (SI: 2.5 - 5) after day 5 suggesting zeolite precipitation may have been a major sink for dissolved calcium limiting its availability for Ca-carbonate mineral precipitation. Siderite ($FeCO_3$) was the only carbonate mineral at equilibrium (log (Q/K)=0) during the M-core experiment.

4.2 Net precipitation and physical changes

The micro-CT analysis provided detailed information on differences between the pre- and post-experimental fractured core. Porosity decreased by 0.5 % and 1 % in the grooved and un-grooved half cores, respectively. A net reduction in porosity and the total grain surface area with a net increase in total grain volume suggested mineral precipitation in both the grooved and un-grooved half cores. The total volume of secondary mineral precipitation is about 1.6 times higher than the volume of primary minerals dissolved in the reacted core. Dissolved and precipitated mineral volumes were higher in the grooved half core compared to the un-grooved half core. The presence of grooves increases the connected porosity and the surface area for fluid-rock interaction, which enhanced the concurrent dissolution and precipitation of minerals in the pores adjacent to the grooves. It seems that the grain surface surrounding the pore was initially exposed to the cation-rich fluid, and over time due to local mineral saturation, precipitation occured primarily within the pores. This process may have partially or fully blocked the pores and initial surface area is changed causing a net increase in grain volume. Precipitation of any mineral is expected to increase the total mineral surface area as early crystals have a high surface area to mass ratio. Aggregates of new minerals are often formed with significant microporosity. These changes in the total mineral

surface area may not be detected as mineral surface area estimates here are limited by the micro-CT image resolution.

There was an approximately even reduction in the number of connected pores and unconnected pores for the bin classes of 0.2 to 0.3 mm and 0.02 to 0.03 mm respectively. A significant reduction of 23 % in the number of pores was observed for the unconnected pores in the reacted sample. However, the throat frequency and the volume of CPN minorly changed. The reduction in pore volume can be attributed to homogeneous precipitation within the pore network, preferentially smectites (due to its higher saturation state). Homogeneous precipitation is a chemical process where minerals precipitate directly from the supersaturated fluid.

Previous studies observed a reduction of the fracture volume due to secondary mineral precipitation upon fluid-rock interaction (Singurindy and Berkowitz 2005, Huerta et al. 2012, Brunet et al. 2016, Jones and Detwiler 2016). Precipitation commences and is particularly prominent in transport-limited zones, where fluid residence time is long enough to reach supersaturation of the fluid with respect to minerals (Oelkers et al. 2008). In a study by Menefee and colleagues (2018), mineral precipitation mostly occurred in the transport limited zones of fractures with a small aperture (<100 µm). Menefee et al. (2018) observed a net reduction of 35 % and 48 % in fracture volume at 100 °C and 150 °C, respectively. Xiong and colleagues (2017) observed 5.4 % and 15 % of a basalts fracture volume was filled with mineral precipitates at 100 and 150 °C, respectively, after 40 weeks of diffusion-controlled reaction. Flow-through studies conducted on an unfractured basalt core at 150 °C and 150 bars observed a net reduction of 0.7 % to 0.8 % porosity (Luhmann et al. 2017a). The above studies have stated that the observed volume reduction in fractures and pores is the result of net precipitation, however, dissolution and precipitation volume was not estimated separately.

The PNM of the un-grooved half core in this study showed a significant reduction in the number of pores compared to pore throats. This is evidence for preferential precipitation within pores and does not much affect the pore connectivity, i.e., pore throats. Pore connectivity is, however, affected by dissolution as the number of isolated pores decreased. What appeared to be isolated pores based on imaging with a resolution of 14.99 µm could have been pores connected by smaller pores and throats, which grew in diameter due to mineral dissolution during the incubation and were classified as connected pores post incubation. The sub-scale features in the solid could have

masked the true volume changes. The invisible pores and throats is just an unfortunate artifact if working with CT data on rocks. Consequently, the number and volume of isolated pores are expected to decrease as observed in our data. While our data suggest precipitation occurs primarily within pores and dissolution affects areas dominated by sub-resolution porosity, the total volume of the CPN only changed by 0.7%.

Fractures increase the connected porosity of a rock, which in turn increases the CO_2 storage capacity of a reservoir (McGrail et al. 2006, Goldberg et al. 2008, Hellevang et al. 2017, Xiong et al. 2017). Therefore, understanding the change in the structure of the connected porosity (CPN) is of importance for estimating the storage capacity of a reservoir. This study shows at least a fraction of pores classified as isolated, based on CT imaging, are involved in fluid-rock interactions and effect properties such as the effective porosity and the surface area of the CPN. Underestimation of the CPN because of the limited image resolution could lead to an incorrect assessment of CO_2 storage potential in fractured reservoirs.

This study focused on diffusion-controlled fluid-rock reactions in the pore network adjacent to fractures in a basalt and observed a significant net reduction in the number of pores and total porosity over a period of 12 weeks. Self-sealing of fractures can only be expected once the adjacent pore network is largely blocked and secondary minerals start to precipitate in advection-dominated fractures. Precipitation rates could be faster in fractures compared to the adjacent pore network if reaction rates are transport-limited in both settings. Interestingly, the volume of the four grooves (~ 518 mm^3) is only around 3x larger than the estimated volume of net mineral precipitation within the analysed area of both core halves (3x 158 = 474 mm^3) within the 12 week reaction period. This comparison suggests that fractures with a similar spacing and aperture, as in the experimental samples, could seal within a few months.

4.4 Capacity of Si consumption into secondary silicate minerals in the initial pore volumes

Based on the micro-CT segmentation, the initial total pore volume is 2042 mm^3 (CPN volume + isolated volume). The net reduction of the initial pore volume over 85 days due to precipitation is 158 mm^3. The mass of ions consumed by the precipitation of secondary minerals can be estimated assuming certain supersaturated minerals precipitate. For example, if only kaolinite ($Al_2Si_2O_5(OH)_4$) with a density of 2.6 g/cm^3 and Si mass per mineral volume of 0.54 g/cm^3

precipitates, then 0.085 g of Si is consumed to form 158 mm^3 of kaolinite. To block the initial CPN volume of 518 mm^3, 0.28g of Si is consumed and 1 g of Si is required to precipitate to block the initial total pore volume of 2042 mm^3. If multiple secondary minerals are formed, for example equal amounts of beidellite (a smectite), a stilbite (a zeolite) and kaolinite, Si mass is shared and in total 0.085 g of Si is consumed for the formation of 158 mm^3 of new solid phase. Such estimates could help to constrain the ionic mass required to fill the fracture and adjacent pore space.

5 Conclusions

Mineral dissolution and precipitation in the pore network adjacent to fractures in a basalt was observed at the pore-scale in an experiment where CO_2-saturated water reacted with basalt fractures and the adjacent pore network at a temperature of 60°C and a pressure of 80 bars over 12 weeks. The fluid was continuously enriched in cations due to mineral dissolution in diffuser bags containing powdered basalt. Changes in the pore network geometry and connectivity were quantified in order to constrain the early processes and conditions leading to changes in the CPN geometry.

X-ray micro-CT analysis showed mineral dissolution and precipitation occurred concurrently with precipitation exceeding dissolution leading to a net increase in grain volume and a decrease in porosity. Specifically, a total of 258 mm^3 of secondary minerals precipitated and 98.4 mm^3 of primary minerals dissolved resulting in a net precipitation of 158 mm^3 over 12 weeks compared to an initial pore volume of 2042 mm^3. The volume of dissolved and precipitated minerals in the grooved half-core was higher than in the un-grooved half-core, because of the larger interface to the adjacent pore network. A reduction in the number of pores was significantly higher compared to throats suggesting mineral precipitation mainly occured in pores. A decline in the number of isolated pores is attributed to mineral dissolution in areas where the pore and throat size was initially below the micro-CT imaging resolution and dissolution enlarged those pore spaces to the extent of becoming detectible. Si-Al minerals including kaolinite, smectite and zeolite and chalcedony were predicted to precipitate based on the fluid composition.

The volume of the CPN only decreased by 0.7 %. This observation is in agreement with unchanged pore throat radii giving further evidence that the early precipitation in pores adjacent to fractures has little impact on pore connectivity and thus permeability.

Acknowledgments

The authors thank the Melbourne Trace Analysis for Chemical, Earth and Environmental Sciences (TrACEES) Platform for access to the phoenix nanotom m micro-CT instrument. The critical evaluation provided by the Editor and the reviewers has improved the impact and clarity of our manuscript.

Data Availability

The raw data for all the experiments and micro-CT analysis has been uploaded to Mendley data and can be accessed at: **https://data.mendeley.com/datasets/n72yhbppkj/1**

References

Adeoye, J. T., A. H. Menefee, W. Xiong, R. K. Wells, P. Skemer, D. E. Giammar and B. R. Ellis (2017). "Effect of transport limitations and fluid properties on reaction products in fractures of unaltered and serpentinized basalt exposed to high PCO2 fluids." International Journal of Greenhouse Gas Control **63**: 310-320

Ahmed, Z. and M. Lebedev (2019). "Elastic properties of sands, Part 1: Micro computed tomography image analysis of grain shapes and their relationship with microstructure." Geophysical Prospecting **67**(4-Rock Physics: from microstructure to seismic signatures): 723-744

Avizo (2018). "Avizo Software 9 User's Guide." 9,

Brunet, J.-P. L., L. Li, Z. T. Karpyn and N. J. Huerta (2016). "Fracture opening or self-sealing: Critical residence time as a unifying parameter for cement–CO 2–brine interactions." International Journal of Greenhouse Gas Control **47**: 25-37

Callow, B., I. Falcon-Suarez, S. Ahmed and J. Matter (2018). "Assessing the carbon sequestration potential of basalt using X-ray micro-CT and rock mechanics." International Journal of Greenhouse Gas Control **70**: 146-156

Doroszko, M. and A. Seweryn (2017). "A new numerical modelling method for deformation behaviour of metallic porous materials using X-ray computed microtomography." Materials Science and Engineering **689**: 142-156

Duan, Z. and R. Sun (2003). "An improved model calculating CO2 solubility in pure water and aqueous NaCl solutions from 273 to 533 K and from 0 to 2000 bar." Chemical Geology **193**(3): 257-271

Eggleton, R. A., C. Foudoulis and D. Varkevisser (1987). "Weathering of Basalt - Changes in Rock Chemistry and Mineralogy." Clays and Clay Minerals **35**(3): 161-169 DOI: 10.1346/Ccmn.1987.0350301

Gharbi, O., B. Bijeljic, E. Boek and M. J. Blunt (2013). "Changes in pore structure and connectivity induced by CO2 injection in carbonates: A combined pore-scale approach." Energy Procedia **37**: 5367-5378

Goldberg, D. S., T. Takahashi and A. L. Slagle (2008). "Carbon dioxide sequestration in deep-sea basalt." Proc Natl Acad Sci U S A **105**(29): 9920-9925 DOI: 10.1073/pnas.0804397105

GWB11 (2016). "Geochemist's workbench (version 11)[software]. Department of Geology at the University of Illinois Urbana Champaign."

Gysi, A. P. and A. Stefánsson (2012c). "Mineralogical aspects of CO 2 sequestration during hydrothermal basalt alteration—An experimental study at 75 to 250 C and elevated pCO 2." Chemical Geology **306**: 146-159

Hellevang, H., B. G. Haile and A. Tetteh (2017). "Experimental study to better understand factors affecting the CO2 mineral trapping potential of basalt." Greenhouse Gases-Science and Technology **7**(1): 143-157 DOI: 10.1002/ghg.1619

Huerta, N. J., M. A. Hesse, S. L. Bryant, B. R. Strazisar and C. L. Lopano (2012). "Experimental evidence for self-limiting reactive flow through a fractured cement core: Implications for time-dependent wellbore leakage." Environmental science & technology **47**(1): 269-275 DOI: 10.1021/es3013003

Jones, T. A. and R. L. Detwiler (2016). "Fracture sealing by mineral precipitation: The role of small- scale mineral heterogeneity." Geophysical Research Letters **43**(14): 7564-7571

Luhmann, A. J., B. M. Tutolo, B. C. Bagley, D. F. Mildner, W. E. Seyfried and M. O. Saar (2017a). "Permeability, porosity, and mineral surface area changes in basalt cores induced by reactive transport of CO2- rich brine." Water Resources Research **53**(3): 1908-1927

Luhmann, A. J., B. M. Tutolo, C. Tan, B. M. Moskowitz, M. O. Saar and W. E. Seyfried (2017b). "Whole rock basalt alteration from CO2-rich brine during flow-through experiments at 150° C and 150bar." Chemical Geology **453**: 92-110 DOI: 10.1016/j.chemgeo.2017.02.002

Matter, J. M., M. Stute, S. O. Snaebjornsdottir, E. H. Oelkers, S. R. Gislason, E. S. Aradottir, B. Sigfusson, I. Gunnarsson, H. Sigurdardottir, E. Gunnlaugsson, G. Axelsson, H. A. Alfredsson, D. Wolff-Boenisch, K. Mesfin, D. Fernandez de la Reguera Taya, J. Hall, K. Dideriksen and W. S. Broecker (2016). "Rapid carbon mineralization for permanent disposal of anthropogenic carbon dioxide emissions." Science **352**(6291): 1312-1314 DOI: 10.1126/science.aad8132

McGrail, B. P., H. T. Schaef, A. M. Ho, Y. J. Chien, J. J. Dooley and C. L. Davidson (2006). "Potential for carbon dioxide sequestration in flood basalts." Journal of Geophysical Research-Solid Earth **111**(B12) DOI: Artn B12201 10.1029/2005jb004169

McGrail, B. P., H. T. Schaef, F. A. Spane, J. B. Cliff, O. Qafoku, J. A. Horner, C. J. Thompson, A. T. Owen and C. E. Sullivan (2016). "Field Validation of Supercritical CO2 Reactivity with Basalts." Environmental Science & Technology Letters,

Menefee, A. H., D. E. Giammar and B. R. Ellis (2018). "Permanent CO2 Trapping through Localized and Chemical Gradient-Driven Basalt Carbonation." Environmental science & technology **52**(15): 8954-8964 DOI: 10.1021/acs.est.8b01814

Oelkers, E. H., S. R. Gislason and J. Matter (2008). "Mineral carbonation of CO2." Elements **4**(5): 333-337

Otsu, N. (1979). "A threshold selection method from gray-level histograms." IEEE transactions on systems, man, and cybernetics **9**(1): 62-66

Phukan, M., H. P. Vu and R. R. Haese (2021). "Mineral dissolution and precipitation reactions and their net balance controlled by mineral surface area: An experimental study on the interactions between continental flood basalts and CO2-saturated water at 80 bars and 60° C." Chemical Geology **559**: 119909

Ramos, K. and K. Matouš (2018). "Micro-computed tomography based experimental investigation of micro-and macro-mechanical response of particulate composites with void growth." Philosophical Magazine **98**(34): 3049-3071

Rogers, K. L., P. S. Neuhoff, A. K. Pedersen and D. K. Bird (2006). "CO2 metasomatism in a basalt-hosted petroleum reservoir, Nuussuaq, West Greenland." Lithos **92**(1-2): 55-82

Safiuddin, M. and N. Hearn (2005). "Comparison of ASTM saturation techniques for measuring the permeable porosity of concrete." Cement and Concrete Research **35**(5): 1008-1013

Singurindy, O. and B. Berkowitz (2005). "The role of fractures on coupled dissolution and precipitation patterns in carbonate rocks." Advances in Water Resources **28**(5): 507-521 DOI: 10.1016/j.advwatres.2005.01.002

Sissmann, O., F. Brunet, I. Martinez, F. o. Guyot, A. Verlaguet, Y. Pinquier and D. Daval (2014). "Enhanced olivine carbonation within a basalt as compared to single-phase experiments: reevaluating the potential of CO2 mineral sequestration." Environmental science & technology **48**(10): 5512-5519 DOI: 10.1021/es405508a

Tutolo, B., A. Luhmann, X. Kong, B. Bagley, D. Alba-Venero, N. Mitchell, M. Saar and W. Seyfried Jr (2020). "Contributions of visible and invisible pores to reactive transport in dolomite." Geochemical Perspectives Letters **14**: 42-46

Wolff-Boenisch, D. and I. Galeczka (2018). "Flow-through reactor experiments on basalt-(sea) water-CO 2 reactions at 90° C and neutral pH. What happens to the basalt pore space under post-injection conditions?" International Journal of Greenhouse Gas Control **68**: 176-190

Xiong, W., R. K. Wells and D. E. Giammar (2017). "Carbon sequestration in olivine and basalt powder packed beds." Environmental science & technology **51**(4): 2105-2112

Xiong, W., R. K. Wells, J. A. Horner, H. T. Schaef, P. A. Skemer and D. E. Giammar (2018). "CO2 Mineral Sequestration in Naturally Porous Basalt." Environmental Science & Technology Letters **5**(3): 142-147 DOI: 10.1021/acs.estlett.8b00047

Xiong, W., R. K. Wells, A. H. Menefee, P. Skemer, B. R. Ellis and D. E. Giammar (2017). "CO2 mineral trapping in fractured basalt." International Journal of Greenhouse Gas Control **66**: 204-217 DOI: 10.1016/j.ijggc.2017.10.003